Regional sources of nitrous oxide over the United States: Seasonal variation and spatial distribution

S. M. Miller,[1] E. A. Kort,[2] A. I. Hirsch,[3] E. J. Dlugokencky,[4] A. E. Andrews,[4] X. Xu,[5] H. Tian,[5] T. Nehrkorn,[6] J. Eluszkiewicz,[6] A. M. Michalak,[7] and S. C. Wofsy[1]

Received 1 October 2011; revised 20 January 2012; accepted 12 February 2012; published 30 March 2012.

[1] This paper presents top-down constraints on the magnitude, spatial distribution, and seasonality of nitrous oxide (N_2O) emissions over the central United States. We analyze data from tall towers in 2004 and 2008 using a high resolution Lagrangian particle dispersion model paired with both geostatistical and Bayesian inversions. Our results indicate peak N_2O emissions in June with a strong seasonal cycle. The spatial distribution of sources closely mirrors data on fertilizer application with particularly large N_2O sources over the US Cornbelt. Existing inventories for N_2O predict emissions that differ substantially from the inverse model results in both seasonal cycle and magnitude. We estimate a total annual N_2O budget over the central US of 0.9–1.2 TgN/yr and an extrapolated budget for the entire US and Canada of 2.1–2.6 TgN/yr. By this estimate, the US and Canada account for 12–15% of the total global N_2O source or 32–39% of the global anthropogenic source as reported by the Intergovernmental Panel on Climate Change in 2007.

Citation: Miller, S. M., et al. (2012), Regional sources of nitrous oxide over the United States: Seasonal variation and spatial distribution, *J. Geophys. Res.*, *117*, D06310, doi:10.1029/2011JD016951.

1. Introduction

[2] Nitrous oxide (N_2O) plays a critical role in both stratospheric ozone depletion and climate change. In the stratosphere, it can react with excited oxygen atoms to produce NO_x radicals which, in turn, can catalyze stratospheric ozone destruction [*Nevison and Holland*, 1997; *Ravishankara et al.*, 2009]. Moreover, N_2O is a potent greenhouse gas with a global warming potential of 300 (on a 100 year timescale) [*Forster et al.*, 2007]. With the continued decline of atmospheric CFC concentrations, N_2O is now the third most important long-lived anthropogenic greenhouse gas in terms of radiative forcing (0.173 W/m^2 in 2009, an 11% increase since 1998) (J. Butler, The NOAA annual greenhouse gas index (AGGI), 2010, http://www.esrl.noaa.gov/gmd/aggi/).

[3] Anthropogenic sources of nitrous oxide include agriculture, fossil fuel combustion, and biomass burning [*California Energy Commission*, 2006; *Denman et al.*, 2007]. Isotopic N_2O measurements suggest that agriculture and associated fertilizer use are the largest anthropogenic N_2O sources globally [*Rahn and Wahlen*, 2000; *Röckmann et al.*, 2003]. The atmospheric lifetime of N_2O is relatively long at about 114 years, and the primary sink of N_2O is loss in the stratosphere [*Montzka*, 2003]. Total annual global emissions (~17.7 TgN/yr) are approximately 40–50% higher than in pre-industrial times and continue to rise [*Denman et al.*, 2007]. As a result, global N_2O mixing ratios have been increasing steadily by about 0.2–0.3% per year (about 0.73 ± 0.06 ppb/year or 3.5 TgN/yr) [*Hirsch et al.*, 2006].

[4] Because of the long lifetime of N_2O, spatial and temporal changes in N_2O mixing ratios are very small and remain challenging to measure accurately. For example, the seasonal cycle at Mace Head, Ireland, is only 0.1% relative to the mean abundance [*Hirsch et al.*, 2006]. The combination of a long lifetime, diffuse sources, and a low signal-to-noise ratio in the measurements means that the N_2O increment due to regional sources is very difficult to estimate and verify [*Hirsch et al.*, 2006]. In addition, the percentage of nitrogen released as N_2O after fertilizer application is very uncertain and ranges from 0%–7% [*Bouwman*, 1996]. The diversity of fertilizer application processes and conditions results in emissions that show large spatial and temporal fluctuations and are difficult to constrain. As a result, existing estimates of N_2O emissions (both magnitudes and seasonal trends) are highly uncertain [*Hirsch et al.*, 2006; *Kort et al.*, 2008, 2010, 2011]. Current emissions estimates over North America, for example, may be too low by as much as a factor of three [*Kort et al.*, 2008, 2010].

[1]Department of Earth and Planetary Sciences, Harvard University, Cambridge, Massachusetts, USA.
[2]Jet Propulsion Laboratory, California Institute of Technology, Pasadena, California, USA.
[3]National Renewable Energy Laboratory, DOE, Golden, Colorado, USA.
[4]Global Monitoring Division, NOAA Earth Systems Research Laboratory, Boulder, Colorado, USA.
[5]School of Forestry and Wildlife Sciences, Auburn University, Auburn, Alabama, USA.
[6]Atmospheric and Environmental Research, Lexington, Massachusetts, USA.
[7]Department of Global Ecology, Carnegie Institution for Science, Stanford, California, USA.

0148-0227/12/2011JD016951

[5] The high degree of uncertainty in N_2O emissions complicates efforts to regulate sources under global and regional climate change agreements. At the global scale, the Kyoto Protocol included N_2O as one of the six greenhouse gases targeted for reductions. Within the US, several state and regional regulations target N_2O emissions as well [*Committee on the Environment and the Northeast International Committee on Energy of the Conference of New England Governors and Eastern Canadian Premiers*, 2001; *Western Climate Initiative*, 2010]. For example, the Midwestern Greenhouse Gas Reduction Accord, an agreement among 6 states in the midwestern US, recommends a 20% reduction in 2005 greenhouse gas emissions by 2020. Advisory group recommendations include N_2O as one of the six targeted categories of species [*Advisory Group to the Midwestern Greenhouse Gas Reduction Accord*, 2009]. Given uncertainties in emissions estimates that are $\sim 20\times$ larger than reduction goals, it is very difficult at present to make reliable baseline inventories and track progress toward designated targets.

[6] Several existing studies provide global to regional-scale constraints on N_2O emissions. *Prinn et al.* [1990], *Hirsch et al.* [2006], *Huang et al.* [2008], and *Kort et al.* [2011] derived top-down emissions constraints over large global regions. More recent studies provide regional-scale emissions estimates over Europe [*Manning et al.*, 2003; *Thompson et al.*, 2011; *Corazza et al.*, 2011; *Manning et al.*, 2011]. Top-down estimates over North America are more limited. *Kort et al.* [2008, 2010] used tall tower and aircraft data to make continental-scale improvements to existing emissions estimates for North America. Multiple studies consistently find northern hemisphere emissions that are significantly higher than existing inventories [*Hirsch et al.*, 2006; *Huang et al.*, 2008; *Kort et al.*, 2008, 2010].

[7] The present paper provides detailed spatial and temporal information on the magnitude of N_2O emissions over the United States at much finer resolution than previously possible. We combine data from a network of tall tower measurements with high-resolution atmospheric simulations to provide regional-scale emissions estimates in time and space, representing important baseline information for greenhouse gas regulation.

2. The Model-Data Framework

2.1. Background to the STILT Model

[8] This study relies on STILT, the Stochastic Time-Inverted Lagrangian Transport Model, for simulations of atmospheric N_2O concentrations. STILT is a particle-following model based strongly on the HYSPLIT model [*Draxler and Hess*, 1998]. STILT releases an ensemble of imaginary air particles from a receptor point, a single location in space and time. For our study, we set up the model to send 100 particles 10 days backward in time following the winds in an assimilated mesoscale meteorological model. The surface sources that these particles encounter are used to calculate the contribution of continental sources seen at the receptor point. In particular, STILT assumes that all surface sources will be well-mixed up to half the modeled boundary layer height. Particles below this height see influence from surface sources while those above do not. STILT then calculates an influence footprint based on the number and duration of particles in this surface layer. The influence footprint, when multiplied by an emissions inventory and summed over all geographic regions, provides an estimate of the continental source signal seen at the receptor. This continental signal is added to a modeled boundary condition (i.e. – the mixing ratio in 'clean' air before reaching North America) to estimate the total mixing ratio seen at the receptor point. The very detailed rendition of mixing ratio fluctuations provided by STILT can be validated against individual measurements taken at the receptor (usually a tall tower or aircraft mission), providing a powerful framework for assessing upwind surface or volume sources. Previous studies have applied STILT to a wide range of atmospheric trace gases, including CO_2, CO, methane, and N_2O [i.e., *Gerbig et al.*, 2003; *Lin et al.*, 2003; *Lin and Gerbig*, 2005; *Matross et al.*, 2006; *Kort et al.*, 2008; *Miller et al.*, 2008; *Gourdji et al.*, 2010; *Thompson et al.*, 2011]. *Lin et al.* [2003] and *Gerbig et al.* [2003] provide a detailed explanation of STILT model theory and structure.

2.2. Underlying Meteorological Drivers

[9] STILT simulations in this study use Weather Research and Forecasting (WRF) assimilated meteorological fields version 2.2 [*Skamarock et al.*, 2005; *Nehrkorn et al.*, 2010] and the Brazilian Regional Atmospheric Modeling System (BRAMS v. 3.2) [*Pielke et al.*, 1992; *Cotton et al.*, 2003; *Sanchez-Ccoyllo et al.*, 2006]. BRAMS simulations (45-km resolution) were only available for the year 2004. The limited STILT-BRAMS runs are complemented by STILT-WRF runs for all time periods.

[10] WRF model simulations use a nested meteorological grid resolution; 10-km resolution wind fields drive particle trajectories over most of the continental US and southern Canada. 40-km resolution wind fields drive trajectories as the particles travel to more distant regions. This nested wind field structure affords higher fidelity source attribution near the receptor while still maintaining reasonable computational costs. *Nehrkorn et al.* [2010] provide a full description of the WRF simulations used in STILT.

[11] BRAMS wind fields (v. 3.2) were based strongly on the Regional Atmospheric Modeling System (RAMS) [*Cotton et al.*, 2003] with several updates: new parameterizations for convection (shallow and deep) and turbulence along with modified diagnostic outputs to ensure mass conservation to very high accuracy. All simulations apply a mass conservation fix from *Medvigy et al.* [2005]. STILT parameterizes boundary layer turbulence as a Markov chain process [*Lin et al.*, 2003], and both WRF and BRAMS use a Grell - Devenyi scheme for convection [*Grell and Devenyi*, 2002]. BRAMS estimates boundary layer height in accordance with *Vogelezang and Holtslag* [1996], and WRF uses a Yonsei University Scheme [*Fast*, 2005]. These two approaches give somewhat different estimates for PBL height and exchange rates (see section 4.1).

2.3. Emissions Inventories

[12] We pair the STILT model with four different N_2O emissions inventories: EDGAR v. 4.0, EDGAR 32FT 2000, GEIA, and the Dynamic Land-Ecosystem Model (DLEM) (see Figure 1). The EDGAR inventories include anthropogenic N_2O sources (including sources from agriculture) on a 0.1° by 0.1° and 1° by 1° longitude-latitude grid, respectively,

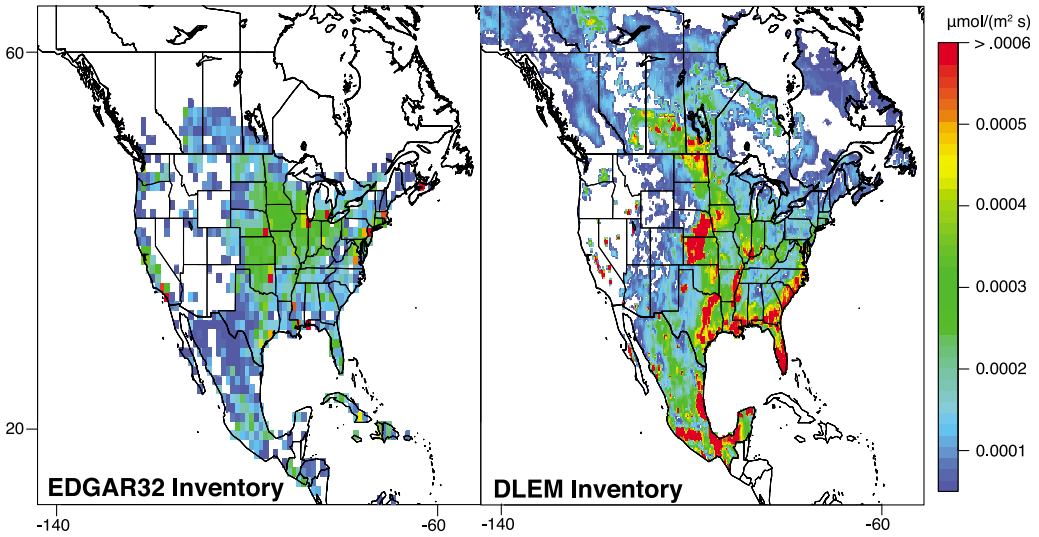

Figure 1. Graphical plots of the different N_2O emissions inventories for 2000. Because DLEM is a daily inventory, the plot above shows average fluxes for May–August 2000. EDGAR v.4 and GEIA (not shown) have similar distributions to EDGAR32 but smaller magnitude (particularly EDGAR v.4).

for v. 4 and 32FT2000 [*Olivier and Peters*, 2005; European Commission, Emission database for global atmospheric research (EDGAR), 2009, http://themasites.pbl.nl/en/themasites/edgar/index.html]. EDGAR v. 4, incorporated into STILT at a $\frac{1}{4}^\circ$ longitude by $\frac{1}{6}^\circ$ latitude resolution, is the more recent, higher-resolution update to EDGAR 32FT2000; while the newer inventory has a similar spatial distribution, the estimated magnitude of fluxes is lower. GEIA incorporates both anthropogenic and natural sources, also on a 1° by 1° grid [*Bouwman et al.*, 1995]. All three inventories are constant in time.

[13] DLEM, a process-based biogeochemical model, estimates N_2O from natural sources and from agriculture [*Tian et al.*, 2010, 2011]. The N_2O model simulates nitrification and denitrification processes as a function of ammonium and nitrate concentrations, soil temperature, and soil moisture. According to *Tian et al.* [2010], DLEM model parameters are then optimized using several Ameriflux sites. Daily emissions estimates are available from 2000–2008 at a 32 km × 32 km resolution (incorporated into STILT on a $\frac{1}{4}^\circ$ by $\frac{1}{6}^\circ$ longitude latitude grid). For all STILT simulations with DLEM, we supplement the inventory with anthropogenic source categories from the EDGAR32FT2000 inventory (i.e. – fossil fuel use, waste handling, water treatment, etc.).

2.4. Model Boundary Condition

[14] The model boundary condition represents N_2O mixing ratios in air that is advected from the Pacific or Arctic Oceans before entering North America. We construct an empirical boundary based on measurements from the NOAA cooperative air sampling network. We use monthly mean dry air mole fractions from 6 monitoring stations (Pacific Ocean stations 5°, 10°, 15°, 20°, 25°, and Barrow, AK) to build a time-varying interpolated boundary at 145°W longitude from the equator to the North Pole. Each particle in the ensemble is assigned a boundary condition mixing ratio based on its ending latitude (projected onto the 145°W boundary). Trajectories that end north of 60° latitude and east of −120° longitude are assigned mixing ratios from a northern boundary condition, constructed from measurements at Alert, Canada, and Summit, Greenland, stations. The estimated boundary condition value assigned to each trajectory is averaged over the entire ensemble to produce the final modeled boundary. This latitudinally, zonally, and temporally varying boundary condition allows the modeled background concentration to change when changing synoptic conditions bring air from different regions of the globe. In contrast to an empirical boundary, we could have used the output from a global chemical tracer model (CTM) for the boundary condition. However, known shortfalls in existing inventories and uncertainties in stratosphere exchange over longer timescales results in CTM N_2O estimates that poorly match measurements [*Kort et al.*, 2011].

[15] Data are insufficient to create a boundary condition for the southern edge of the model domain. Weekly N_2O measurements at Barbados in fall 2008 suggest that the boundary concentration estimated for the WKT tower using our Pacific boundary condition could be too low by up to ∼0.2 ppb. A low estimated boundary at WKT would imply a higher N_2O increment from continental sources. As a result, the flux estimates presented here could consequently be biased slightly high over the southern US, likely by no more than 25%.

[16] The STILT model does not explicitly account for dilution of N_2O due to the influence of stratospheric air. Stratosphere-to-troposphere exchange reaches a maximum during fall through spring and occurs at a much smaller magnitude during summer [*Holton et al.*, 1995; *Sprenger and Wernli*, 2003]. This exchange could influence concentrations at the receptor sites in two very general ways: through broad-scale exchange that becomes well-mixed in the troposphere and through specific "deep exchange" (stratospheric intrusion) events. Broad-scale exchange that becomes well-mixed should be captured by the measurement-based boundary condition. It would be very difficult to account for deep

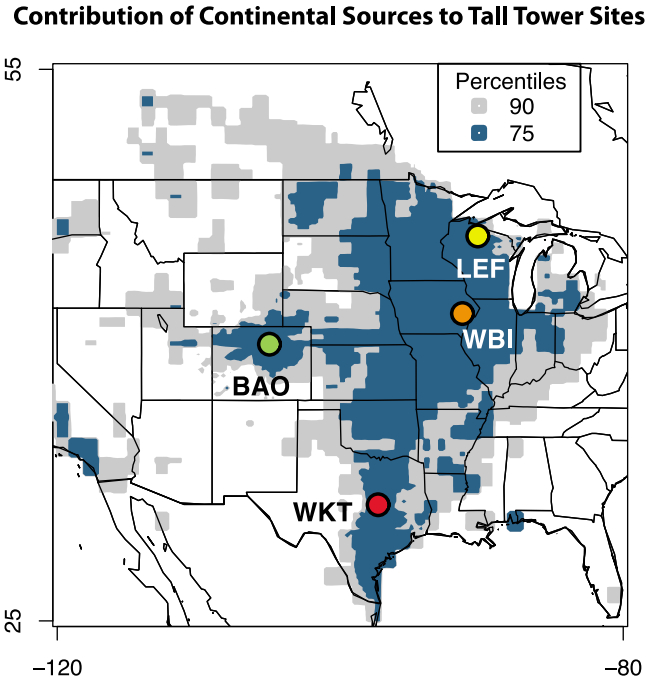

Figure 2. The contour lines indicate the regions that contribute 75 and 90% of the mixing ratio signal seen at each of the tall tower sites. The plot reflects the months of May through August, 2008, and was constructed using the EDGAR32FT2000 emissions inventory. The tall tower ensemble sees influence from N_2O sources over much of the central US.

exchange events, but several indicators might downplay the importance of these events on eventual surface source constraints. First, deep exchange events reach a maximum over the Gulf of Alaska and southern Greenland, areas far from anticipated N_2O sources [*Sprenger and Wernli*, 2003]. Secondly, any depletion due to deep exchange would result in low measurements and modeled concentrations that are too high. This is the opposite of what we see in the actual model (see section 4.4). Finally, the measurements rarely drop below the adjusted modeled boundary condition, suggesting a lack of strong stratospheric influence at the surface sites (e.g., Figures 3 and 8).

2.5. Data Overview

[17] We use two different types of measurement data in the analysis of N_2O emissions: continuous measurements from LEF tower in Wisconsin and daily flask measurements from an ensemble of tall tower sites (Figure 2).

[18] Continuous hourly averaged measurements of N_2O are available only at NOAA's LEF tower site for 5 months (May–Oct.) in 2004. Despite the limited time frame, the data nonetheless provide a high resolution test to validate the STILT-N_2O model. Measurements at LEF were taken using a gas chromatograph [*Hurst et al.*, 1997, 1998] and had an approximate uncertainty of 0.6 ppb. In order to mitigate significant noise in the hourly averaged data, we apply a 4th order, 22-point Savitsky-Golay moving average filter [*Savitzky and Golay*, 1964]. The filter effectively preserves the magnitude of peaks and troughs on synoptic timescales in the time series and substantially decreases noise.

[19] In addition to continuous tall tower measurements, we also draw on a network of daily flask measurements from 4 tall tower sites during 2008. These sites include LEF in Park Falls, Wisconsin (244 m above ground level); WBI in West Branch, Iowa (379 m agl); WKT in Moody, Texas (457 m agl); and BAO in Erie, Colorado (300 m agl). The daily flask data set begins in 2008 with limited data for 2007. We conduct model simulations for the tall tower ensemble over 2008 when both data and meteorological simulations are available. All flask samples were measured using a gas chromatograph and electron capture detector and had a reproducibility of approximately 0.3 ppb. For both hourly and daily data sets, the measurement uncertainty is 30–60% of the typical signal from continental surface sources, making it particularly challenging to derive regional source constraints.

3. Emissions Estimation Methods

3.1. Simple Inventory Optimization

[20] We first discuss data analysis using a simple optimization of each emissions inventory (i.e., GEIA, EDGAR, and DLEM). We plot modeled mixing ratios against measurements and fit a linear regression. Variability in the modeled and/or measured signals should result from the transport of varying sources from different regions. Hence, the regression slope provides an approximate corrective scaling factor for each emissions inventory based on the array of model results and measurement sites. In addition, the intercept of the regression can be interpreted as an additive correction to the modeled boundary condition. We use a reduced major axis (RMA) method [*Miller and Kahn*, 1967] to produce a single scaling factor for each inventory (calculated over all available towers) for each month in 2008 and for each month of the available 2004 LEF data set (using WRF and BRAMS winds separately). An RMA regression accounts for uncorrelated variance in both the x and y axes. The surface source signal over the central US is dominated by fluxes from agriculture (globally ~4× the fossil fuel source) [*Denman et al.*, 2007]; agricultural and urban sources are also co-located in some regions, and therefore we cannot reliably decouple different source types.

[21] The RMA regression provides the most straightforward snapshot of seasonality in N_2O emissions. Significant gaps in the data occur at several towers in 2008, specifically in the winter, spring, and fall months. As such, it is difficult to produce a reliable spatially variant inversion for time periods other than summer of 2008. Therefore, we use the regression method to estimate month-by-month constraints over all of the tower sites.

[22] We apply a boundary correction to each monthly inversion simulation based on the regression intercept. The tall tower data that most strongly constrains the boundary correction are nearly disjoint from data points that constrain the sources, so this procedure has little effect on our main results. If we do not apply a boundary condition correction, the inversions produce obvious bias in the model-data comparisons and unrealistic spatial distributions of the flux fields (e.g., large emissions over the sea or distant regions).

3.2. Geostatistical and Bayesian Inversions

[23] We use both a geostatistical inversion [*Snodgrass and Kitanidis*, 1997; *Michalak et al.*, 2004] and the more

conventional Bayesian approach [*Rodgers*, 2000]. The Bayesian inversion incorporates an a priori emissions inventory, along with the measurements, model results, and uncertainty estimates. The resulting emissions inventory optimization (the a posteriori solution) reflects both the a priori estimate and the model/measurements [*Rodgers*, 2000]. In many applications, the a priori emissions estimate provides important, independent information for the inversion, and the inversion improves upon this initial best guess. In other applications, it can be useful to estimate trace gas emissions more directly from the atmospheric data without the help of an a priori estimate (i.e., making as few initial assumptions as possible). The geostatistical approach is an inversion that can do just that by using a non-informative prior. A geostatistical inversion can be most useful when a priori inventories differ substantially in either magnitude or spatial structure, as is the case for N_2O, indicating significant errors in the spatial distribution of emissions. In this case, the a posteriori solution will vary arbitrarily depending on the highly subjective choice of the prior. It makes sense to learn as much as possible about N_2O fluxes before convolving the results with the influence of a potentially erroneous prior. When different priors give very disparate flux estimates, the geostatistical inversion can inform the choice of prior for a Bayesian inversion or help to describe the spatial distribution of emissions using information directly from atmospheric data.

[24] In this study, the geostatistical approach helps us examine spatial patterns in fluxes independent of disparate a priori inventories (i.e., DLEM versus EDGAR32FT2000). We conducted separate geostatistical inversions for each month during the peak period of fluxes (May–July 2008) on a resolution of 1° latitude × 1° longitude to minimize spatial aggregation errors. We focus on the summer time period because the flask data set was much more sporadic at other times of year. Section 3.3 provides a more mathematically rigorous description of the geostatistical approach.

[25] We also conducted comparable monthly Bayesian inversions during the same time period (May–July 2008). We use the geostatistical method to help inform our choice of a priori inventory and then use the Bayesian method to improve on this best initial inventory estimate.

3.3. Inversion Mathematics

[26] The STILT trace gas model can be written in linear form as follows [*Gerbig et al.*, 2003]:

$$\boldsymbol{z} = \mathbf{H}\boldsymbol{s} + \boldsymbol{b} + \varepsilon \tag{1}$$

$\boldsymbol{z}$ is an $n \times 1$ vector of measurements at the receptor location(s) (in this case, from a tall tower), $\boldsymbol{s}$ is an $m \times 1$ vector of fluxes over the entire model domain, and $\boldsymbol{b}$ is an $n \times 1$ vector that represents the model boundary condition. $\mathbf{H}$, the Jacobian matrix (dimensions $n \times m$), relates the surface fluxes to the continental source signal as measured at the tower. Each column of $\mathbf{H}$ describes the statistical influence of fluxes in a certain grid box on the tall tower site (also known as the "influence footprint"). In other words, the influence footprint converts the emissions inventory from a flux to a mixing ratio increment seen at the receptor. This footprint is calculated based on the number of particles that pass over the grid box and the amount of time the particles spend in the box. $\mathbf{H}\boldsymbol{s}$ ($n \times 1$) represents the contribution of continental sources to the mixing ratio at the receptor (in ppb). $\boldsymbol{\varepsilon}$ is the model-data mismatch: error caused by model transport, model resolution, uncertainties in the measurements, and boundary condition uncertainties (e.g., *Gerbig et al.* [2003], *Matross et al.* [2006], or *Gourdji et al.* [2010] for the STILT model).

[27] The solution to the inverse problem minimizes the chi-squared cost function, somewhat similar to a weighted sum of squares approach. Equations (2) and (3) give the cost function for the Bayesian and geostatistical inversions, respectively.

$$J(\boldsymbol{s}) = \frac{1}{2}(\boldsymbol{z} - \mathbf{H}\boldsymbol{s})^T\mathbf{R}^{-1}(\boldsymbol{z} - \mathbf{H}\boldsymbol{s}) + \frac{1}{2}(\boldsymbol{s} - \boldsymbol{s_a})^T\mathbf{Q}^{-1}(\boldsymbol{s} - \boldsymbol{s_a}) \tag{2}$$

$$J(\boldsymbol{s}, \boldsymbol{\beta}) = \frac{1}{2}(\boldsymbol{z} - \mathbf{H}\boldsymbol{s})^T\mathbf{R}^{-1}(\boldsymbol{z} - \mathbf{H}\boldsymbol{s}) + \frac{1}{2}(\boldsymbol{s} - \mathbf{X}\boldsymbol{\beta})^T\mathbf{Q}^{-1}(\boldsymbol{s} - \mathbf{X}\boldsymbol{\beta}) \tag{3}$$

$\mathbf{R}$ is the $n \times n$ model-data mismatch covariance matrix, and $\mathbf{Q}$ is the $m \times m$ a priori covariance matrix.

[28] The two inversion approaches differ in their treatment of the a priori model. The Bayesian method determines the solution with the maximum probability given the prior estimate and the observations and their range of uncertainties, defined by $\mathbf{R}$ and $\mathbf{Q}$, respectively [*Rodgers*, 2000]. The geostatistical method does not include an a priori inventory ($\boldsymbol{s_a}$) but instead uses a model of the mean ($\mathbf{X}\boldsymbol{\beta}$). Each column of the matrix $\mathbf{X}$ ($m \times p$) can describe possible spatial trends in the data. $\boldsymbol{\beta}$ is a $p \times 1$ vector of unknown drift coefficients that scale the columns of $\mathbf{X}$. This model of the mean could, for example, include information such as land use patterns or population density (i.e. – "auxiliary variables" [see *Gourdji et al.*, 2008]). In this study, however, we use do not use external information in the model of the mean. In other words $\mathbf{X}$ is an $m \times 1$ vector of ones, an uninformative prior. In this case, the unknown value of $\boldsymbol{\beta}$ is the a posteriori mean of the flux field. We want to learn as much as possible about the fluxes from the atmospheric data alone without the aid of any prescribed spatial distribution. Instead, the geostatistical method incorporates broad-scale information within the covariance matrices about the spatial correlation structure of the fluxes. The diagonal elements of $\mathbf{Q}$ define the spatial variance of the fluxes, and the off-diagonal elements of $\mathbf{Q}$ describe the anticipated spatial covariance of the fluxes [e.g., *Snodgrass and Kitanidis*, 1997; *Michalak et al.*, 2004; *Mueller et al.*, 2008].

[29] For both inversions, we include the 90% influence region (see section 4.1) in the inversion area as well as all land area further west. The data do not fully constrain emissions as far away as the West Coast, but we included the West to avoid biasing the a posteriori flux field due to the cumulative effect of distant emissions. We excluded water bodies from the inversion. Globally, the ocean is a significant source of N_2O, diffusely spread over large areas [*Nevison et al.*, 2004; *Denman et al.*, 2007]. However, any fluxes assigned to the ocean by the inversion would more likely reflect boundary condition uncertainties than actual sources and our boundary condition correction should account for the effects of any broad-scale coastal upwelling fluxes.

Table 1. Covariance Matrix Parameters for the Geostatistical and Bayesian Inversions

	σ_{R_MAY}	σ_{R_JUN}	σ_{R_JUL}	l (km)	σ_Q
Geostatistical	0.71 ± 0.05	0.97 ± 0.05	0.70 ± 0.04	816 ± 313	$(4.5 \pm 3) \times 10^{-4}$
Bayesian	0.72 ± 0.05	0.99 ± 0.05	0.73 ± 0.04	816 ± 313	$(3.7 \pm 2) \times 10^{-4}$

[30] The analytical solutions to both Bayesian and geostatistical inversions are calculated via a system of linear equations. The solution to the Bayesian approach for the STILT model is described by *Gerbig et al.* [2003] and *Miller et al.* [2008], and the solution to the geostatistical inversion is described in detail by *Snodgrass and Kitanidis* [1997] and *Michalak et al.* [2004].

3.4. Covariance Matrices

[31] The covariance matrices (**Q** and **R**) provide crucial information that describes the structure of the a posteriori flux field and/or the relative uncertainties in the inversion inputs. These matrices must be estimated independent of the inversion and are often inferred from the atmospheric data itself [*Kitanidis and Lane*, 1985; *Kitanidis*, 1995; *Michalak et al.*, 2005]. Mathematically, the individual elements of **R** and **Q** are defined as follows:

$$R_{i,j}\left(t_{i,j}|\sigma_R, t_R\right) = \sigma_R^2 \exp\left(-\frac{t_{i,j}}{t_R}\right) \tag{4}$$

$$Q_{i,j}\left(h_{i,j}|\sigma_Q, l\right) = \sigma_Q^2 \exp\left(-\frac{h_{i,j}}{l}\right) \tag{5}$$

σ_R^2, the diagonal elements of **R**, represent the variance of the errors caused by model-data mismatch. This includes uncertainties due to the measurements, the forward model, model representation (e.g., aggregation of discreet flux regions), and uncertainties in the boundary condition. In this case, we estimate a single model-data mismatch error over all towers for each month. The off-diagonal elements are the covariances which decay exponentially in time ($t_{i,j}$) according to the temporal decorrelation in model-data mismatch errors (t_R). We constructed a first order autoregressive model on the difference between model and measurements and found a decorrelation time of 4–10 h for hourly data at LEF with the WRF model (depending on the data interpolation method used). This is smaller than the daily measurement frequency in the ensemble data, so we do not include temporal correlations in model-data mismatch (off-diagonal elements of **R**). We also assume zero error correlation among observations at different tower sites.

[32] The a priori covariance matrix takes on a similar form. For the geostatistical inversion, the diagonal elements (σ_Q^2) give the anticipated variance of the fluxes, and for the Bayesian inversion, they describe the uncertainty in the a priori inventory. The off-diagonal elements of **Q** decay exponentially with distance ($h_{i,j}$) according to the decorrelation length parameter (l). In the case of the geostatistical inversion, l describes spatial correlation in the flux field while for the Bayesian inversion, l describes the spatial correlation of uncertainties in the a priori inventory. Spatial correlation becomes negligible at distance $3l$.

[33] We infer most of the covariance matrix parameters from the atmospheric data itself using Maximum Likelihood (ML) and Restricted Maximum Likelihood (RML) methods. In this case, we apply the RML method to infer geostatistical inversion parameters [*Kitanidis*, 1995; *Snodgrass and Kitanidis*, 1997] and the ML method to infer Bayesian inversion parameters [*Kitanidis and Lane*, 1985; *Michalak et al.*, 2005]. These closely related techniques provide objective ways to infer any number of inversion parameters. The most likely parameters are those that minimize a given cost function and are normally estimated using an iterative Gauss-Newton algorithm. ML and RML ensure that the reduced chi-squared value of both the model/measurements and fluxes are close to one. This implies that the errors in the a posteriori model are consistent with those estimated by the covariance parameters [e.g., *Michalak et al.*, 2005]. It is important to note, however, that ML and RML can produce unreliable inversion parameters when either the data are sparse or the model/measurement errors are large [*Mueller et al.*, 2008; *Gourdji et al.*, 2010].

[34] This latter concern becomes important in the inversion setup here. In cases where we cannot infer inversion parameters from the atmospheric data, we infer these values from auxiliary data sets. For example, we assume that the posterior fluxes and errors in the a priori inventory will be correlated over a length scale (l) similar to that of agricultural land use patterns (inferred from cropland maps using RML in kriging form) [*Mueller et al.*, 2008; *Ramankutty et al.*, 2008]. Existing emissions inventories of N_2O, corrected in magnitude in accordance with *Kort et al.* [2008], provide an estimate of σ_Q for the geostatistical inversion (again using RML in kriging form). Additionally, we use the difference between the standard and corrected inventory from *Kort et al.* [2008] for σ_Q in the Bayesian setup. Table 1 lists the full set of parameters used in the geostatistical and Bayesian setups.

4. Results and Discussion

4.1. Model Results: An Overview

[35] The STILT model appears very adept at reproducing high resolution N_2O concentration data for a range of different receptor sites. The hourly data from LEF Tower in 2004 demonstrate the model's ability to reproduce high resolution measurements (see Figure 3). In this case, we ran the model using both the WRF and BRAMS meteorological drivers. STILT achieves model-measurement correlation as high as $R = 0.76$ (for EDGAR32FT2000), though correlations for other inventories can be lower ($R = 0.48$ for DLEM) (see Table 2). The time series in Figure 3 displays the model result for both the BRAMS and WRF-driven models after optimization.

[36] Before fully discussing the source optimization results, it is first important to highlight the differences in STILT model runs with BRAMS versus WRF meteorological drivers. In general, the BRAMS runs produce a slightly better model-measurement fit than WRF ($R = 0.76$ and 0.73, respectively, for EDGAR32FT2000), though this difference in fit is only

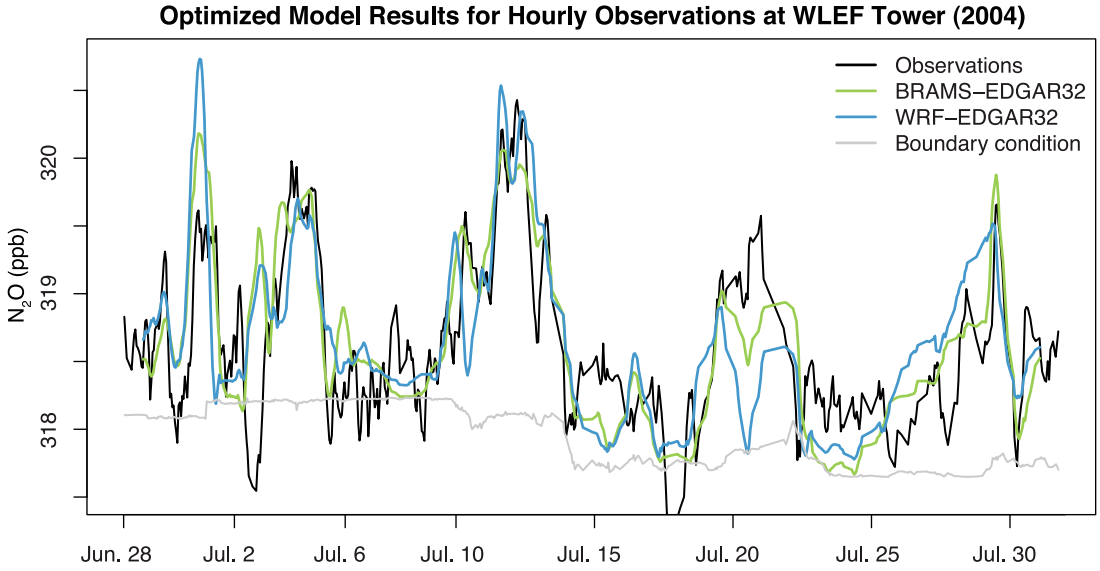

Figure 3. STILT model results for hourly observations at LEF Tower in Park Falls, WI, with two different meteorological drivers. Each result is optimized with a reduced major axis regression and smoothed with a Savitsky-Golay filter.

significant in the cases of EDGAR32 and GEIA ($p = 0.01$ in both cases). Secondly, when using the same flux fields, STILT-WRF runs produce modeled mixing ratios that are systematically lower than those produced by STILT-BRAMS, statistically significant for all inventories. This difference appears to stem from the fact that particle trajectories in WRF-driven simulations reach greater altitudes more quickly than in BRAMS simulations and therefore see the influence of surface sources over a shorter interval. For example, in Figure 4, the average influence footprint of WRF and BRAMS simulations is initially the same. However, the surface influence drops to lower values on days 2–4 for WRF, likely because particles move out of the planetary boundary layer (PBL) a bit faster, and thus lower mixing ratios modeled at the receptor. During the first day, and in the far field, the footprints are similar and the overall mean footprints differ by 15–20%.

[37] WRF and BRAMS also display different nighttime mixed layer heights (~30 m for WRF and 250 m for BRAMS). STILT can set systematically different nighttime mixed layer heights, and differences in estimated concentrations among model versions with different nighttime mixed layers appears to be minimal. Resolution of the discrepancy in particle heights between WRF and BRAMS is beyond the scope of this paper but would be a significant subject to improve the transport model uncertainties.

[38] In addition to differences in meteorology, we also examined possible differences in the model during the afternoon versus nighttime at LEF in 2004. We optimized mid-afternoon (18–23 UTC) and nighttime (6–14 UTC) data points separately using the RMA regression for each month and each meteorological driver. The inventory correction factors were usually similar, within 5% for afternoon versus nighttime measurements and almost never differed by more than 15%. Evidently, agricultural sources affecting LEF are large area sources and are dominated by synoptic-scale flow.

[39] The emissions constraints presented here apply mostly to the Great Plains corridor and western Great Lakes of the United States. Figure 2 shows the mean "regions of influence" for the 2008 tall tower ensemble model runs. At each geographic grid square, we multiply the footprint by the EDGAR 32FT2000 emissions inventory. The result is the mixing ratio increment that each grid cell contributes to the measured signal at the tall tower site. The contour lines provide an estimate of the geographic regions that contribute 75 and 90% of the mean trace gas signal seen at the tall tower sites. Figure 2 shows that the 2008 tall tower ensemble is most sensitive to fluxes across the central

Table 2. Emissions Inventory Correction Factors and Model-Measurement Correlation Coefficients for 2004 Calculated Using an RMA Regression Based on Hourly LEF Tower Nitrous Oxide Measurements

		Inventory Correction Factors						
Inventory	Meteorology	May	Jun	Jul	Aug	Sep	Oct	R
EDGAR32FT2000	BRAMS	2.5 ± 0.2	2.6 ± 0.1	1.5 ± 0.1	1.5 ± 0.1	1.3 ± 0.1	1.4 ± 0.1	0.76
	WRF	3.7 ± 0.2	3.4 ± 0.2	1.6 ± 0.2	1.9 ± 0.2	1.2 ± 0.1	1.4 ± 0.1	0.73
EDGARv4	BRAMS	4.4 ± 0.3	4.8 ± 0.3	2.6 ± 0.2	2.7 ± 0.2	2.3 ± 0.2	2.5 ± 0.2	0.76
	WRF	6.2 ± 0.3	6.1 ± 0.4	2.7 ± 0.2	3.5 ± 0.3	2.2 ± 0.2	2.4 ± 0.2	0.74
GEIA	BRAMS	3.7 ± 0.2	4.1 ± 0.2	2.5 ± 0.2	2.3 ± 0.2	2.0 ± 0.2	1.9 ± 0.1	0.76
	WRF	5.1 ± 0.3	5.5 ± 0.4	2.4 ± 0.2	2.9 ± 0.3	1.8 ± 0.2	2.0 ± 0.2	0.73
DLEM	BRAMS	1.7 ± 0.1	1.1 ± 0.1	0.90 ± 0.1	0.66 ± 0.06	0.50±0.05	1.3 ± 0.1	0.52
	WRF	2.2 ± 0.2	1.3 ± 0.1	0.85 ± 0.06	0.94 ± 0.09	0.63±0.06	1.1 ± 0.1	0.48

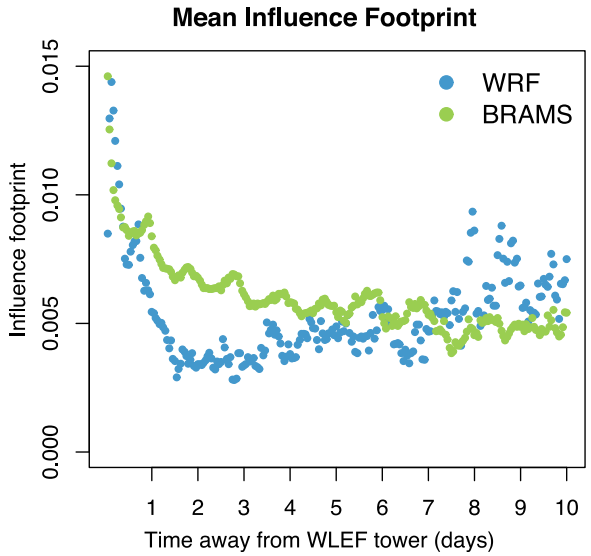

Figure 4. The mean footprint of particles (in ppm/μmol m^{-2} s^{-1}) by time away from the LEF tower (2004) for both BRAMS and WRF. BRAMS sees a larger footprint than WRF between 0.5–6 days away from the tower.

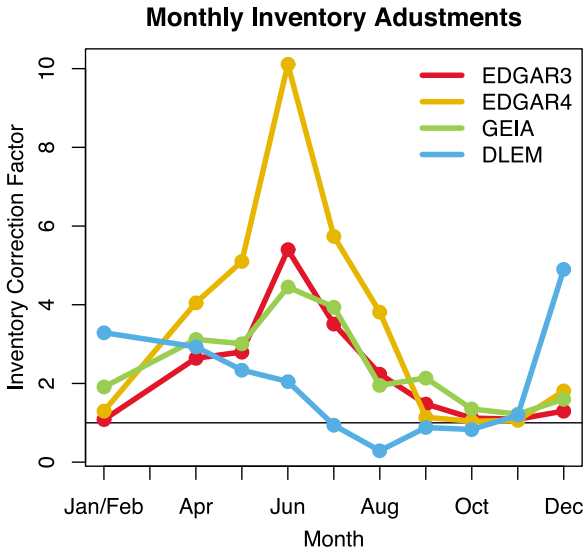

Figure 5. Corrective emissions inventory scaling factors produced by the RMA regression for the ensemble of 2008 tall tower data.

corridor of the United States. A similar plot for the 2004 LEF data set (not shown) produces a region of influence that covers the corn belt and northern plains states. Hence, the model inversions that follow in this paper predominantly provide constraints for the central US.

4.2. Seasonality of N_2O Emissions

[40] We construct a reduced major axis regression for the 2008 daily tall tower ensemble data in order to make broad monthly corrections to existing inventories (see Table 3). Figure 5 shows the monthly emissions inventory corrections taken over the entire ensemble of all tower sites. Note that January and February are lumped together because there were only 15 days of model runs for the former month. Also, we did not compute an inventory correction for March because two of the four towers did not report any data.

[41] The results from the entire ensemble provide important information about the seasonal cycle of N_2O over the central US in 2008. Note that since DLEM is a daily inventory, it includes estimated seasonality while GEIA and the EDGAR inventories only provide yearly emissions totals. Our study shows strongly seasonal fluxes that peak in June and fall off at similar rates on either side of the peak. The scaling factors for DLEM represent corrections to the seasonality already included in the inventory. These scalers indicate that DLEM overestimates fluxes during late summer relative to other months and slightly underestimates sources early in the year. The DLEM adjustment for December is anomalous. The inventory in December is 25% lower than in either November of January, and inventory sources during this month shift somewhat eastward, explaining the anomaly at least in part.

[42] Modeled footprints change slightly from one month to another, and some months lack measurements from one or more towers. Hence, scaling factors for each month could be weighted toward certain regions because of missing towers or seasonal changes in synoptic transport. As a result, the above constraints represent both seasonal changes in surface sources and any artifacts from data availability and seasonal footprint variations.

4.3. Location of N_2O Emissions

[43] Different N_2O emissions inventories exhibit very different spatial patterns (see Figure 1). EDGAR inventories place the largest sources over the US Cornbelt (i.e., Iowa, Illinois, etc.) while DLEM places high emissions in more westerly (e.g., Kansas and Nebraska) and southerly areas (e.g., Texas, Arkansas, Kansas). The geostatistical inversion provides a very transparent way to learn about the spatial distribution of the fluxes based on atmospheric data independent of existing emissions inventories. We conducted the geostatistical inversion for three different months (May–July, 2008) using STILT-WRF.

[44] Figure 6 shows the a posteriori flux fields for May, June, and July, along with associated a posteriori uncertainties as estimated by the geostatistical inversion. We conducted the inversion over a large region that includes most of the

Table 3. Emissions Inventory Correction Factors for 2008 Calculated Using an RMA Regression Based on an Ensemble of Tall Towers

	Inventory Correction Factors									
Inventory	Jan/Feb	Apr	May	Jun	Jul	Aug	Sep	Oct	Nov	Dec
EDGAR32	1.1 ± 0.1	2.6 ± 0.4	2.8 ± 0.4	5.4 ± 0.6	3.5 ± 0.4	2.2 ± 0.3	1.5 ± 0.3	1.1 ± 0.2	1.1 ± 0.2	1.3 ± 0.2
EDGARv4	1.3 ± 0.2	4.1 ± 0.7	5.1 ± 0.7	10.1 ± 1.2	5.7 ± 0.7	3.8 ± 0.5	1.14 ± 0.2	1.0 ± 0.2	1.1 ± 0.2	1.8 ± 0.3
GEIA	1.9 ± 0.2	3.1 ± 0.5	3.0 ± 0.5	4.5 ± 0.7	3.9 ± 0.6	2.0 ± 0.3	2.1 ± 0.4	1.4 ± 0.2	1.2 ± 0.2	1.6 ± 0.2
DLEM	3.3 ± 0.4	2.9 ± 0.5	2.3 ± 0.4	2.1 ± 0.3	0.9 ± 0.1	0.29 ± 0.04	0.88 ± 0.18	0.83 ± 0.13	1.2 ± 0.2	4.9 ± 0.7

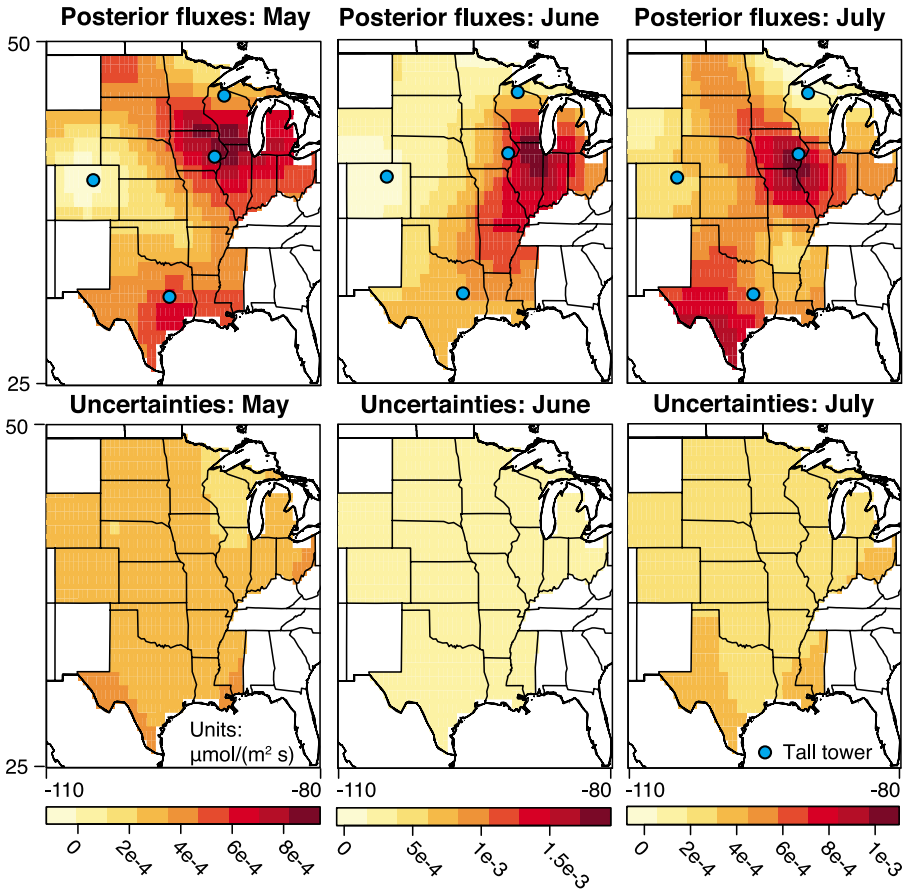

Figure 6. Monthly a posteriori fluxes and associated uncertainties (a posteriori standard deviations) estimated for the geostatistical inversion. This plot is made using different colors from Figure 1 and on different scales to better highlight spatial trends.

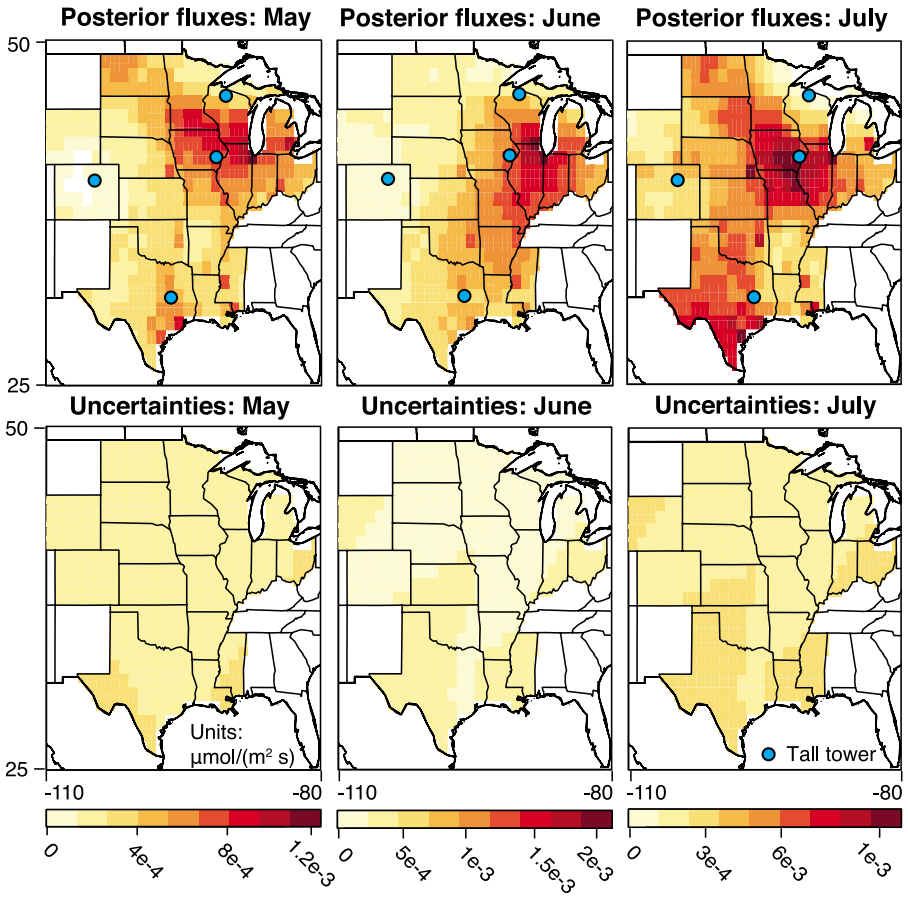

Figure 7. The a posteriori source estimates for N_2O using the EDGAR32FT2000 inventory in a Bayesian inversion framework (for May – July 2008). Each month is plotted on a different scale to better highlight spatial patterns.

continental US and Canada but show results only for the area within the 75% influence region of the tower sites (see Figure 6). The results of the inversion strongly indicate large N_2O sources over the US Corn Belt (i.e., Iowa, Illinois, etc.). This source region continues to the northwest into North Dakota with a diminished magnitude, and emissions taper off quickly moving westward into Colorado, Wyoming, and the western Plains States.

[45] With limited atmospheric data, the Bayesian inversion cannot fully correct discrepancies in spatial distribution among inventories. In this case, the geostatistical inversion can inform our choice of a priori inventory. Based both on the geostatistical simulations and the 2004 measurement-model correlations, we select EDGAR32FT2000 as the best a priori inventory for the Bayesian inversion. The EDGAR inventories and GEIA place major sources over the Corn Belt, in agreement with the geostatistical simulations, while DLEM places the largest sources elsewhere. The EDGAR and GEIA inventories also produce the highest model-measurement fit (R^2), and EDGAR32FT2000, in specific, requires less magnitude correction than either GEIA or EDGAR v. 4.

4.4. Magnitude of N_2O Emissions

[46] The following section details the results of the Bayesian inversion to improve upon existing N_2O emissions inventories and details estimated emissions budgets from the variety of statistical methods. While the geostatistical setup aimed to discern large scale spatial patterns, the Bayesian setup described here leverages the best existing inventory to produce a more spatially resolved estimate of fluxes. The inversion was conducted for May, June, and July, the months with peak N_2O fluxes and with nearly complete tall tower data sets. Figure 7 plots the EDGAR32FT2000 a posteriori

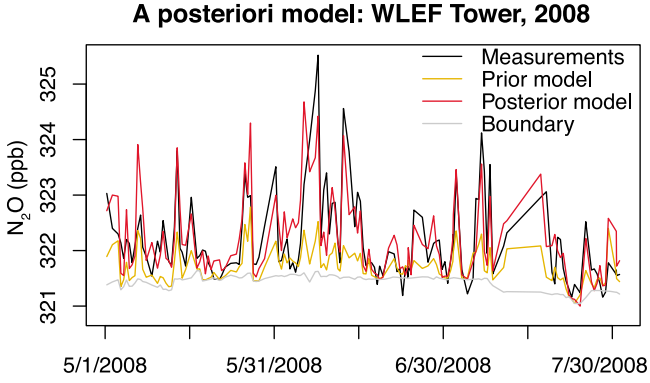

Figure 8. An example of the STILT model result at LEF tower with both the a priori and a posteriori EDGAR32FT2000 inventories.

Table 4. N_2O Budget Information for 2004 and 2008 Data Sets for the Inversion Region Shown in Figure 5 (in TgN/Month)[a]

	May	Jun	Jul	Aug	Sep	Oct
LEF Tower 2004 (RMA)	0.12–0.18	0.12–0.19	0.073–.089	0.073–0.11	0.056–0.068	0.065–0.075
Ensemble 2008 (RMA)	0.11–0.15	0.16–0.29	0.14–0.17	0.070–0.11	0.032–0.074	0.031–0.054
Ensemble 2008 (Geostatistical)	0.11 ± 0.08	0.18 ± 0.08	0.13 ± 0.07			
Ensemble 2008 (Bayesian)	0.11 ± 0.07	0.18 ± 0.06	0.13 ± 0.06			

[a]The ranges in 2004 and 2008 RMA reflect different inventories and meteorological drivers while 2008 geostatistical- and Bayesian-derived budgets include a posteriori uncertainties calculated by the respective inversions.

inventory from the Bayesian inversion, and Figure 8 shows an example of the modeled time series from the LEF tower. The results look somewhat similar to the geostatistical setup but are less dispersive and have more spatial detail.

[47] The inversions and regressions suggest sources that are significantly larger than in either EDGAR or GEIA for nearly all geographic regions and times of year. Interestingly, estimated emissions in the newest release of EDGAR (v. 4) are lower than previous releases, requiring even larger modification. Table 4 displays monthly N_2O budgets from the inversions and RMA regressions for both 2004 and 2008. Using the RMA regression for the 2008 ensemble of tall tower sites, we estimate an annual N_2O budget of 1.0–1.2 TgN/yr for the inversion region. If we divide these results by the percentage of fluxes in the inversion region (see Table 5), we can extrapolate to the entire US and Canada. The resulting budget estimate for the United States and Canada is 2.4–2.6 TgN/yr. This range of estimates reflects the results of different starting inventories (the EDGAR and GEIA inventories). The different methods produce slightly different budget estimates, in some part due to uncertainties in the boundary condition. The inversions, for example, apply a single boundary condition correction for the entire summer period whereas the regressions calculate a unique intercept for each month.

[48] Differences in the meteorological drivers modestly widen the uncertainty bounds on the budget estimate. Optimal fluxes on average were 12% lower when using BRAMS. The mean scaling factor for EDGAR 2000 over the year is 2.2 for WRF and 1.8 for BRAMS. If we extrapolate to the 2008 data set, this result suggests that BRAMS would yield a budget of ~1 TgN/yr over the central US and ~2.2 TgN/yr over the US and Canada.

[49] The budget numbers presented here compare well to those estimated in previous top-down studies over North America, notably those by *Kort et al.* [2008, 2010]. These studies estimated a US and Canada N_2O budget of 0.23 TgN/month for spring and summer months in 2003 and 2004. This compares to a peak June US and Canada budget of ~0.22–0.35 TgN/yr presented here across a variety of different source optimization methods. Our annual budget number for the US and Canada corresponds to 13–15% of the total global source, or 36–39% of the global anthropogenic source (12–13% and 32–34% using BRAMS, respectively) as reported by the IPCC [*Denman et al.*, 2007].

Table 5. The Percentage of a Priori N_2O Fluxes in the United States and Canada That Lie Within the Inversion Region as Displayed in Figure 6

	EDGAR32	EDGAR v.4	GEIA	DLEM
Percentage (%)	51	48	40	39

5. Conclusions

[50] This study captures nitrous oxide sources over the agricultural belt of the United States at more highly resolved spatial and temporal scales than previous estimates. A diverse set of statistical tools, from a simple regression to Bayesian and geostatistical inversions, provide a closer look at three different aspects of emissions: seasonality, location, and intensity. The largest sources appear over the US Cornbelt (i.e., Iowa, Illinois, Indiana, southern Minnesota, etc.) with smaller sources likely extending into the Dakotas. This result is consistent with the spatial patterns in the EDGAR and GEIA inventories. N_2O emissions peak in June and taper off quickly both before and after, a seasonality largely missing from existing inventories. The choice of meteorology for the transport model had a significant influence (12 ± 6%) on the estimated total emissions, with relatively

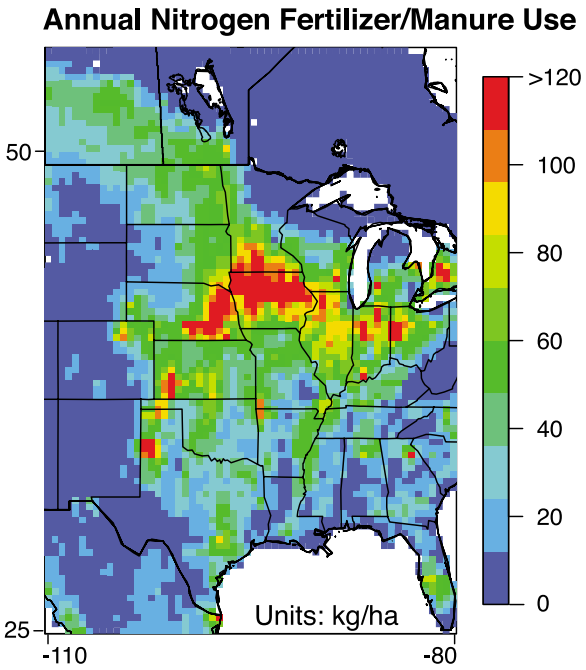

Figure 9. An estimate of annual fertilizer use taken from *Potter et al.* [2010]. The a posteriori N_2O fluxes from both the geostatistical and Bayesian inversions are strongly similar to the spatial distribution of nitrogen fertilizer. *Potter et al.* [2010] estimate manure application for 2007 and synthetic fertilizer for 2000.

small effect on our derived spatial distribution and little impact on the derived seasonal variation. We estimate a budget over the central US of 1.0–1.2 TgN/yr using WRF meteorology (0.9–1.1 using BRAMS), a source that is notably larger than the EDGAR and GEIA inventories. Of particular note, the newest release of EDGAR (v. 4), decreases the source strength over previous EDGAR estimates, a revision that is inconsistent with the atmospheric data.

[51] The sources inferred from the tall tower measurements show striking similarity to the anticipated spatial and temporal distributions of fertilizer application and corn production, supporting the view that fertilizer plays a dominant role in generating N_2O emissions over the central US (see Figure 9). Both fertilizer use and N_2O emissions correspond strongly with the distribution of corn production (not shown), likely due to the magnitude of corn production and high fertilizer use relative to other crops (Food and Agriculture Organization of the United Nations, Plant Production Protection Division, Fertistat: Fertilizer Use Statistics, 2007, http://www.fao.org/ag/agl/fertistat/; USDA National Agricultural Statistics Service, Charts and Maps, County Maps, 2010, http://www.nass.usda.gov/Charts_and_Maps/Crops_County/index.asp). Given this correspondence between corn and N_2O, the potential for significant agricultural greenhouse gas emissions are important to consider when weighing the costs and benefits of corn subsidies and ethanol production.

[52] **Acknowledgments.** This work was supported by the American Meteorological Society Graduate Student Fellowship/DOE Atmospheric Radiation Measurement Program, the DOE Computational Science Graduate Fellowship, and the National Science Foundation Graduate Research Fellowship Program. We thank Marcos Longo and Elaine Gottlieb (Harvard) for their help with model meteorology. The generation of the WRF meteorological fields was supported by the National Aeronautics and Space Administration (NASA) under grants NNX06AE84G, NNH05CC42C, and NNX08AR47G; National Science Foundation grant ATM-0836153; and NOAA/ESRL contracts RA133R-08-SE-2359 and NRMJ1000-15617DT. The WRF and STILT runs described in this paper have been made possible by access to NASA's high-end computing resources and we thank the personnel at the NASA Ames supercomputing facility for technical assistance. Additionally, we thank Kimberly Mueller and Sharon Gourdji (Carnegie Institution for Science) for input on the Restricted Maximum Likelihood implementation, and we thank Navin Ramankutty and Philip Potter (McGill University) for their fertilizer use data sets.

References

Advisory Group to the Midwestern Greenhouse Gas Reduction Accord (2009), Final draft recommendations, report, Midwestern Gov. Assoc., Washington, D. C. [Available at http://www.igreenlaw.com/storage/Final_Model_Rule1.pdf.]

Bouwman, A. F. (1996), Direct emission of nitrous oxide from agricultural soils, *Nutr. Cycl. Agroecosyst.*, *46*(1), 53–70, doi:10.1007/BF00210224.

Bouwman, A. F., K. W. Vanderhoek, and J. G. J. Olivier (1995), Uncertainties in the global source distribution of nitrous-oxide, *J. Geophys. Res.*, *100*(D2), 2785–2800.

California Energy Commission (2006), Inventory of California greenhouse gas emissions and sinks: 1990 to 2004, *CEC-600-2006-0123-SF*, Calif. Energy Comm., Sacramento.

Committee on the Environment and the Northeast International Committee on Energy of the Conference of New England Governors and Eastern Canadian Premiers (2001), Climate change action plan 2001, report, Boston, Mass. [Available at http://www.cleanair-coolplanet.org/information/pdf/2001_Climate_Action_Plan.pdf.]

Corazza, M., P. Bergamaschi, A. Vermeulen, T. Aalto, L. Haszpra, F. Meinhardt, S. Doherty, and R. Thompson (2011), Inverse modelling of European N_2O emissions: Assimilationg observations from different networks, *Atmos. Chem. Phys.*, *11*, 2381–2398, doi:10.5194/acp-11-2381-2011.

Cotton, W. R., et al. (2003), RAMS 2001: Current status and future directions, *Meteorol. Atmos. Phys.*, *82*(1–4), 5–29, doi:10.1007/s00703-001-0584-9.

Denman, K., et al. (2007), *Couplings Between Changes in the Climate System and Biogeochemistry*, Cambridge Univ. Press, Cambridge, U. K.

Draxler, R. R., and G. D. Hess (1998), An overview of the HYSPLIT 4 modelling system for trajectories, dispersion, and deposition, *Aust. Meteorol. Mag.*, *47*, 295–308.

Fast, J. (2005), Evaluation of the boundary layer characteristics and particulates in mexico city predicted by WRF, paper presented at WRF/MM5 Users' Workshop, Natl. Cent. for Atmos. Res., Boulder, Colo.

Forster, P., et al. (2007), *Changes in Atmospheric Constituents and in Radiative Forcing*, Cambridge Univ. Press, Cambridge, U. K.

Gerbig, C., J. C. Lin, S. C. Wofsy, B. C. Daube, A. E. Andrews, B. B. Stephens, P. S. Bakwin, and C. A. Grainger (2003), Toward constraining regional-scale fluxes of CO_2 with atmospheric observations over a continent: 2. Analysis of COBRA data using a receptor-oriented framework, *J. Geophys. Res.*, *108*(D24), 4757, doi:10.1029/2003JD003770.

Gourdji, S. M., K. L. Mueller, K. Schaefer, and A. M. Michalak (2008), Global monthly averaged CO_2 fluxes recovered using a geostatistical inverse modeling approach: 2. Results including auxiliary environmental data, *J. Geophys. Res.*, *113*, D21115, doi:10.1029/2007JD009733.

Gourdji, S. M., A. I. Hirsch, K. L. Mueller, V. Yadav, A. E. Andrews, and A. M. Michalak (2010), Regional-scale geostatistical inverse modeling of North American CO_2 fluxes: A synthetic data study, *Atmos. Chem. Phys.*, *10*(13), 6151–6167, doi:10.5194/acp-10-6151-2010.

Grell, G. A., and D. Devenyi (2002), A generalized approach to parameterizing convection combining ensemble and data assimilation techniques, *Geophys. Res. Lett.*, *29*(14), 1693, doi:10.1029/2002GL015311.

Hirsch, A. I., A. M. Michalak, L. M. Bruhwiler, W. Peters, E. J. Dlugokencky, and P. P. Tans (2006), Inverse modeling estimates of the global nitrous oxide surface flux from 1998–2001, *Global Biogeochem. Cycles*, *20*, GB1008, doi:10.1029/2004GB002443.

Holton, J. R., et al. (1995), Stratosphere-troposphere exchange, *Rev. Geophys.*, *33*(4), 403–439, doi:10.1029/95RG02097.

Huang, J., et al. (2008), Estimation of regional emissions of nitrous oxide from 1997 to 2005 using multinetwork measurements, a chemical transport model, and an inverse method, *J. Geophys. Res.*, *113*, D17313, doi:10.1029/2007JD009381.

Hurst, D. F., P. S. Bakwin, R. C. Myers, and J. W. Elkins (1997), Behavior of trace gas mixing ratios on a very tall tower in North Carolina, *J. Geophys. Res.*, *102*(*D7*), 8825–8835.

Hurst, D. F., P. S. Bakwin, and J. W. Elkins (1998), Recent trends in the variability of halogenated trace gases over the United States, *J. Geophys. Res.*, *103*(D19), 25,299–25,306.

Kitanidis, P. K. (1995), Quasi-linear geostatistical theory for inversing, *Water Resour. Res.*, *31*(10), 2411–2419.

Kitanidis, P. K., and R. W. Lane (1985), Maximum-likelihood parameter-estimation of hydrologic spatial processes by the Gauss-Newton method, *J. Hydrol.*, *79*(1–2), 53–71.

Kort, E. A., et al. (2008), Emissions of CH_4 and N_2O over the United States and Canada based on a receptor-oriented modeling framework and COBRA-NA atmospheric observations, *Geophys. Res. Lett.*, *35*, L18808, doi:10.1029/2008GL034031.

Kort, E. A., et al. (2010), Atmospheric constraints on 2004 emissions of methane and nitrous oxide in North America from atmospheric measurements and receptor-oriented modeling framework, *J. Integr. Environ. Sci.*, *7*(2), 125–133, doi:10.1080/19438151003767483.

Kort, E. A., et al. (2011), Tropospheric distribution and variability of N_2O: Evidence for strong tropical emissions, *Geophys. Res. Lett.*, *38*, L15806, doi:10.1029/2011GL047612.

Lin, J. C., and C. Gerbig (2005), Accounting for the effect of transport errors on tracer inversions, *Geophys. Res. Lett.*, *32*, L01802, doi:10.1029/2004GL021127.

Lin, J. C., C. Gerbig, S. C. Wofsy, A. E. Andrews, B. C. Daube, K. J. Davis, and C. A. Grainger (2003), A near-field tool for simulating the upstream influence of atmospheric observations: The Stochastic Time-Inverted Lagrangian Transport (STILT) model, *J. Geophys. Res.*, *108*(D16), 4493, doi:10.1029/2002JD003161.

Manning, A. J., D. B. Ryall, R. G. Derwent, P. G. Simmonds, and S. O'Doherty (2003), Estimating European emissions of ozone-depleting and greenhouse gases using observations and a modeling back-attribution technique, *J. Geophys. Res.*, *108*(D14), 4405, doi:10.1029/2002JD002312.

Manning, A. J., S. O'Doherty, A. R. Jones, P. G. Simmonds, and R. G. Derwent (2011), Estimating UK methane and nitrous oxide emissions from 1990 to 2007 using an inversion modeling approach, *J. Geophys. Res.*, *116*, D02305, doi:10.1029/2010JD014763.

Matross, D. M., et al. (2006), Estimating regional carbon exchange in New England and Quebec by combining atmospheric, ground-based and satellite data, *Tellus, Ser. B*, *58*(5), 344–358, doi:10.1111/j.1600-0889.2006.00206.x.

Medvigy, D., P. R. Moorcroft, R. Avissar, and R. L. Walko (2005), Mass conservation and atmospheric dynamics in the regional atmospheric

modeling system (RAMS), *Environ. Fluid Mech.*, *5*(1–2), 109–134, doi:10.1007/s10652-005-5275-5.

Michalak, A. M., L. Bruhwiler, and P. P. Tans (2004), A geostatistical approach to surface flux estimation of atmospheric trace gases, *J. Geophys. Res.*, *109*, D14109, doi:10.1029/2003JD004422.

Michalak, A. M., A. Hirsch, L. Bruhwiler, K. R. Gurney, W. Peters, and P. P. Tans (2005), Maximum likelihood estimation of covariance parameters for Bayesian atmospheric trace gas surface flux inversions, *J. Geophys. Res.*, *110*, D24107, doi:10.1029/2005JD005970.

Miller, R. L., and J. S. Kahn (1967), *Statistical Analysis in the Geological Sciences*, John Wiley, Hoboken, N. J.

Miller, S. M., et al. (2008), Sources of carbon monoxide and formaldehyde in North America determined from high-resolution atmospheric data, *Atmos. Chem. Phys.*, *8*(24), 7673–7696, doi:10.5194/acp-8-7673-2008.

Montzka, S. (2003), Controlled substances and other source gases, in *Scientific Assessment of Ozone Depletion: 2002*, edited by A.-L. Nohende Ajavon et al., pp. 1.1–1.83, World Meteorol. Org., Geneva, Switzerland.

Mueller, K. L., S. M. Gourdji, and A. M. Michalak (2008), Global monthly averaged CO_2 fluxes recovered using a geostatistical inverse modeling approach: 1. Results using atmospheric measurements, *J. Geophys. Res.*, *113*, D21114, doi:10.1029/2007JD009734.

Nehrkorn, T., J. Eluszkiewicz, S. C. Wofsy, J. C. Lin, C. Gerbig, M. Longo, and S. Freitas (2010), Coupled Weather Research and Forecasting–Stochastic Time-Inverted Lagrangian Transport (WRF-STILT) model, *Meteorol. Atmos. Phys.*, *107*(1–2), 51–64, doi:10.1007/s00703-010-0068-x.

Nevison, C., and E. Holland (1997), A reexamination of the impact of anthropogenically fixed nitrogen on atmospheric N_2O and the stratospheric O_3 layer, *J. Geophys. Res.*, *102*(D21), 25,519–25,536.

Nevison, C. D., T. J. Lueker, and R. F. Weiss (2004), Quantifying the nitrous oxide source from coastal upwelling, *Global Biogeochem. Cycles*, *18*, GB1018, doi:10.1029/2003GB002110.

Olivier, J. G. J., and J. Peters (2005), CO_2 from non-energy use of fuels: A global, regional and national perspective based on the IPCC tier 1 approach, *Resour. Conserv. Recycl.*, *45*(3), 210–225, doi:10.1016/j.resconrec. 2005.05.008.

Pielke, R. A., et al. (1992), A comprehensive meteorological modeling system—RAMS, *Meteorol. Atmos. Phys.*, *49*(1–4), 69–91.

Potter, P., et al. (2010), Characterizing the spatial patterns of global fertilizer application and manure production, *Earth Interact.*, *14*, 1–11, doi:10.1175/2009EI288.1.

Prinn, R., D. Cunnold, R. Rasmussen, P. Simmonds, F. Alyea, A. Crawford, P. Fraser, and R. Rosen (1990), Atmospheric emissions and trends of nitrous-oxide deduced from 10 years of ale-gauge data, *J. Geophys. Res.*, *95*(D11), 18,369–18,385.

Rahn, T., and M. Wahlen (2000), A reassessment of the global isotopic budget of atmospheric nitrous oxide, *Global Biogeochem. Cycles*, *14*(2), 537–543.

Ramankutty, N., A. T. Evan, C. Monfreda, and J. A. Foley (2008), Farming the planet: 1. Geographic distribution of global agricultural lands in the year 2000, *Global Biogeochem. Cycles*, *22*, GB1003, doi:10.1029/2007GB002952.

Ravishankara, A. R., J. S. Daniel, and R. W. Portmann (2009), Nitrous oxide (N_2O): The dominant ozone-depleting substance emitted in the 21st century, *Science*, *326*(5949), 123–125, doi:10.1126/science.1176985.

Röckmann, T., J. Kaiser, and C. A. M. Brenninkmeijer (2003), The isotopic fingerprint of the pre-industrial and the anthropogenic N_2O source, *Atmos. Chem. Phys.*, *3*, 315–323, doi:10.5194/acp-3-315-2003.

Rodgers, C. (2000), *Inverse Methods for Atmospheric Sounding: Theory and Practice*, World Sci., Singapore.

Sanchez-Ccoyllo, O. R., P. L. Silva Dias, M. D. Andrade, and S. R. Freitas (2006), Determination of O_3^-, CO^- and PM10- transport in the metropolitan area of Sao Paulo, Brazil through synoptic-scale analysis of back trajectories, *Meteorol. Atmos. Phys.*, *92*(1–2), 83–93, doi:10.1007/s00703-005-0139-6.

Savitzky, A., and M. J. E. Golay (1964), Smoothing and differentiation of data by simplified least squares procedures, *Anal. Chem.*, *36*(8), 1627–1639, doi:10.1021/ac60214a047.

Skamarock, W., J. Klemp, J. Dudhia, D. Gill, D. Barker, W. Wang, and J. Powers (2005), A description of the advanced research WRF version 2, *NCAR/TN468+STR*, 100 pp., Natl. Cent. for Atmos. Res., Boulder, Colo.

Snodgrass, M. F., and P. K. Kitanidis (1997), A geostatistical approach to contaminant source identification, *Water Resour. Res.*, *33*(4), 537–546.

Sprenger, M., and H. Wernli (2003), A northern hemispheric climatology of cross-tropopause exchange for the ERA15 time period (1979–1993), *J. Geophys. Res.*, *108*(D12), 8521, doi:10.1029/2002JD002636.

Thompson, R., C. Gerbig, and C. Roedenbeck (2011), A Bayesian inversion estimate of N_2O emissions for western and central Europe and the assessment of aggregation errors, *Atmos. Chem. Phys.*, *11*, 3443–3458, doi:10.5194/acp-11-3443-2011.

Tian, H., X. Xu, M. Liu, W. Ren, C. Zhang, G. Chen, and C. Lu (2010), Spatial and temporal patterns of CH_4 and N_2O fluxes in terrestrial ecosystems of North America during 1979–2008: Application of a global biogeochemistry model, *Biogeosciences*, *7*(9), 2673–2694, doi:10.5194/bg-7-2673-2010.

Tian, H., X. Xu, C. Lu, M. Liu, W. Ren, G. Chen, J. Melillo, and J. Liu (2011), Net exchanges of CO_2, CH_4, and N_2O between China's terrestrial ecosystems and the atmosphere and their contributions to global climate warming, *J. Geophys. Res.*, *116*, G02011, doi:10.1029/2010JG001393.

Vogelezang, D. H. P., and A. A. M. Holtslag (1996), Evaluation and model impacts of alternative boundary-layer height formulations, *Boundary Layer Meteorol.*, *81*(3–4), 245–269.

Western Climate Initiative (2010), Design for the WCI regional program, report, Sacramento, Calif.

A. E. Andrews and E. J. Dlugokencky, Global Monitoring Division, NOAA Earth Systems Research Laboratory, 325 Broadway R/GMD1, Boulder CO 80305–3328, USA. (arlyn.andrews@noaa.gov; ed.dlugokencky@noaa.gov)

J. Eluszkiewicz and T. Nehrkorn, Atmospheric and Environmental Research, 131 Hartwell Ave., Lexington, MA 02421, USA. (jeluszki@aer.com; tnehrkor@aer.com)

A. I. Hirsch, National Renewable Energy Laboratory, DOE, MS R202, 1617 Cole Blvd., Golden, CO 80401, USA. (adam.hirsch@nrel.gov)

E. A. Kort, Jet Propulsion Laboratory, California Institute of Technology, MS 233–300, 4800 Oak Grove Dr., Pasadena, CA 91109, USA. (kort47@gmail.com)

A. M. Michalak, Department of Global Ecology, Carnegie Institution for Science, 260 Panama St., Stanford, CA 94305, USA. (michalak@stanford.edu)

S. M. Miller and S. C. Wofsy, Department of Earth and Planetary Sciences, Harvard University, 20 Oxford St., Cambridge, MA 02138, USA. (smiller@fas.harvard.edu; swofsy@seas.harvard.edu)

H. Tian and X. Xu, School of Forestry and Wildlife Sciences, Auburn University, 602 Duncan St., Auburn, AL 36849, USA. (tianhan@auburn.edu; xuxiaof@tigermail.auburn.edu)